

Local viscosity distribution in bifurcating microfluidic blood flows

Cite as: Phys. Fluids **30**, 030706 (2018); <https://doi.org/10.1063/1.5011373>

Submitted: 31 October 2017 . Accepted: 30 January 2018 . Published Online: 16 February 2018

E. Kaliviotis , J. M. Sherwood , and S. Balabani 

COLLECTIONS

Paper published as part of the special topic on [Papers from the 8th Meeting of the Hellenic Society of Rheology](#)



View Online



Export Citation



CrossMark

ARTICLES YOU MAY BE INTERESTED IN

[Instability of two-layer film flows due to the interacting effects of surfactants, inertia, and gravity](#)

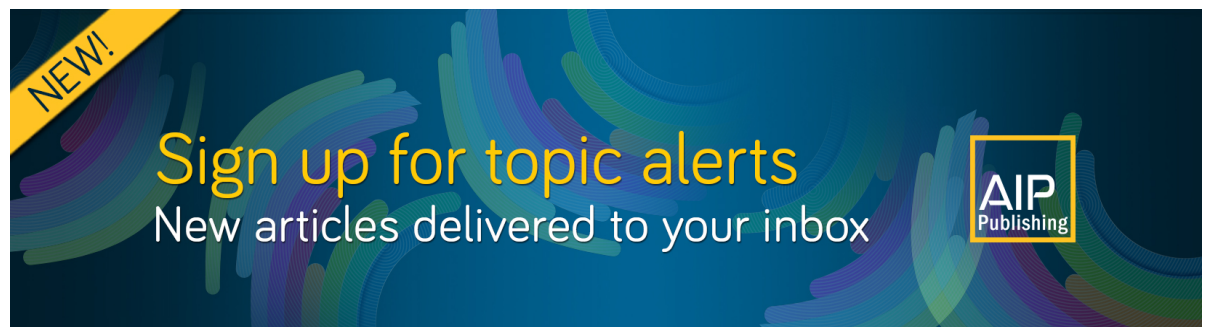
Physics of Fluids **30**, 030707 (2018); <https://doi.org/10.1063/1.5010896>

[A constitutive rheological model for agglomerating blood derived from nonequilibrium thermodynamics](#)

Physics of Fluids **30**, 030710 (2018); <https://doi.org/10.1063/1.5016913>


[Analysis of red blood cell partitioning at bifurcations in simulated microvascular networks](#)

Physics of Fluids **30**, 051902 (2018); <https://doi.org/10.1063/1.5024783>



NEW!

Sign up for topic alerts
New articles delivered to your inbox



Local viscosity distribution in bifurcating microfluidic blood flows

E. Kaliviotis,^{1,2,a)} J. M. Sherwood,³ and S. Balabani²

¹*Department of Mechanical Engineering and Material Science and Engineering, Cyprus University of Technology, Limassol 3041, Cyprus*

²*Department of Mechanical Engineering, University College London, London WC1E 6BT, United Kingdom*

³*Department of Bioengineering, Imperial College London, London SW7 2AZ, United Kingdom*

(Received 31 October 2017; accepted 30 January 2018; published online 16 February 2018)

The red blood cell (RBC) aggregation phenomenon is majorly responsible for the non-Newtonian nature of blood, influencing the blood flow characteristics in the microvasculature. Of considerable interest is the behaviour of the fluid at the bifurcating regions. *In vitro* experiments, using microchannels, have shown that RBC aggregation, at certain flow conditions, affects the bluntness and skewness of the velocity profile, the local RBC concentration, and the cell-depleted layer at the channel walls. In addition, the developed RBC aggregates appear unevenly distributed in the outlets of these channels depending on their spatial distribution in the feeding branch, and on the flow conditions in the outlet branches. In the present work, constitutive equations of blood viscosity, from earlier work of the authors, are applied to flows in a T-type bifurcating microchannel to examine the local viscosity characteristics. Viscosity maps are derived for various flow distributions in the outlet branches of the channel, and the location of maximum viscosity magnitude is obtained. The viscosity does not appear significantly elevated in the branches of lower flow rate as would be expected on the basis of the low shear therein, and the maximum magnitude appears in the vicinity of the junction, and towards the side of the outlet branch with the higher flow rate. The study demonstrates that in the branches of lower flow rate, the local viscosity is also low, helping us to explain why the effects of physiological red blood cell aggregation have no adverse effects in terms of *in vivo* vascular resistance. *Published by AIP Publishing.* <https://doi.org/10.1063/1.5011373>

I. INTRODUCTION

Microfluidics has enabled microscale blood transport phenomena to be resolved in greater detail that has been achieved hitherto and hence shed light to many fundamental aspects of the microcirculation. The microvasculature is a complex network of microvessels in which the various blood constituents [with the red blood cell (RBC) dominating at proportions of 40%-45%] are circulated in an inertialess flow environment (Reynolds number <1). The cellular nature of blood in combination with the microvasculature architecture results in (a) the non-uniform distribution of the RBCs (both in the flow and cross-flow directions, due to the plasma skimming and the migration phenomenon of RBCs) and (b) a cell-depleted layer formed at the walls of the vessels (Secomb, 2017). Both these phenomena have a profound impact on the velocity and rheological characteristics of the fluid (Pries and Secomb, 2003), as they result in the reduction of RBC concentration as the flow is directed to smaller vessels (the Fahraeus effect), and, as a consequence, a reduction of the apparent viscosity of the fluid therein (the Fahraeus-Lindqvist effect) (Lipowsky *et al.*, 1980b).

Microscale blood flow characteristics can be examined *in vitro* by combining microscopic imaging techniques (mainly brightfield and confocal) with micro particle image

(or tracking) velocimetry (μ PIV and μ PTV, respectively). A number of such studies have been conducted employing straight and bifurcating rectangular microchannels and providing detailed velocity information; it has been shown that the velocity profile is blunted in the central regions of the flow (Lima *et al.*, 2006; 2008b; and Kaliviotis *et al.*, 2016a) and skewed downstream of the bifurcations (Leble *et al.*, 2011; Sherwood *et al.*, 2012b; and 2014). The observed velocity characteristics have been shown to closely relate to the local haematocrit (Lima *et al.*, 2008a and Sherwood *et al.*, 2014). Studies in more complicated bifurcating geometries, such as T-junctions, have shown that the bluntness and skewness of the velocity and haematocrit profiles are affected by the flow ratio between the outlet branches, and that an inverse relationship exists between the flow ratio and the aforementioned quantities (Sherwood *et al.*, 2012b; 2014). A structural characteristic of particular interest for microscale blood flows is the cell-depleted layer (CDL) formed near the walls of the flow configuration due to RBC lateral migration. It has been shown that a CDL forms in the straight section and increases in width at the outlet branches of bifurcating geometries depending on the proportion of the flow rate in the branch relative to the parent branch (flow ratio therein) (Lima *et al.*, 2008b; Sherwood *et al.*, 2012a; Brands *et al.*, 2013; and Sampaio *et al.*, 2015).

RBC aggregation has been found to affect all the aforementioned characteristics of microscale blood flows at certain flow conditions: velocity bluntness and skewness, haematocrit distribution, CDL, and viscosity (Sherwood *et al.*,

^{a)}Email: e.kaliviotis@cut.ac.cy

2012a; 2012b; 2014; Kaliviotis *et al.*, 2016a; 2016b; and 2017). RBC aggregation is a physiological phenomenon; however, it is found significantly elevated in various pathologies because of its sensitivity to inflammation-sensitive proteins (mainly fibrinogen). The distribution of aggregates in microscale blood flows has been recently quantified using image processing techniques; it has been shown that, in general, the size of aggregates in the flow is exponentially distributed (Mehri *et al.*, 2014 and Kaliviotis *et al.*, 2017). Furthermore, the distribution of aggregates in bifurcations has been found to be influenced by their spatial distribution in the feeding branch and by the flow conditions in the outlets of the bifurcation (Kaliviotis *et al.*, 2017).

RBC aggregation is majorly responsible for the Non-Newtonian and viscoelastic nature of blood. This fact has been extensively investigated in the literature and blood constitutive equations and models of varying complexity have been proposed in the literature (Yilmaz and Gundogdu, 2008). Local viscosity characteristics, however, have not received particular attention for microscale blood flows. The most substantial attempt to characterise blood viscosity in the microcirculation is perhaps that of Pries and co-workers (1992; 2005), who—based on experimental observations—developed a model describing the viscosity of blood in terms of arteriole diameter and the haematocrit therein, taking into consideration the cell-depleted layer near the vessel walls. Long *et al.* (2004) and Damiano *et al.* (2004) also attempted to quantify the viscosity of blood in glass tubes and microvessels of the mouse cremaster muscle, respectively; the viscosity profile in the venules of the cremaster muscle was derived from the velocity distribution assuming Newtonian, Poiseuille flow. Koutsiaris measured velocity (2016a) and estimated wall shear stresses (2016b) in the living human eye microcirculation by employing particle tracking techniques. An attempt to map the local viscosity characteristics of microscale blood flows has been made by the authors previously, employing two different viscosity models (Kaliviotis *et al.*, 2011 and Sherwood *et al.*, 2012b). In the first study, a viscosity model described in Kaliviotis and Yianneskis (2009; 2011), which incorporates secondary aggregation effects (i.e., aggregate network formation), was employed. The viscosity field was calculated based on the in-plane shearing fields and the local haematocrit observed in a plate-plate shearing system demonstrating considerable spatial variation of viscosity in the microscale. In a subsequent study by Sherwood *et al.* (2012b), the Pries *et al.* (1992) viscosity model was applied to the microscale blood flows in a T-junction geometry and the viscosity distribution was characterised in the outlet branches of the microchannel. The study showed considerable variation of viscosity in the cross-flow direction, commensurate with the haematocrit distribution therein, as the Pries model dictates.

In the present work, the viscosity characteristics of blood flow in a T-junction microchannel are examined further by using the viscosity model developed earlier by the authors. Viscosity fields are produced and the location of maximum viscosity is identified for a range of flow distributions within the microchannel. The results are compared against those obtained by the Pries model.

II. METHODS

This section provides a brief but comprehensive description of the methods employed in the study. For more details on the experimental apparatus, sample preparation, and flow measurement techniques, the reader is referred to our previous studies (Sherwood *et al.*, 2012a; 2012b). The methodology for aggregate size characterization is detailed in the studies of Kaliviotis *et al.* (2016a; 2017) and the viscosity model used for the calculation of the viscosity field in Kaliviotis and Yianneskis (2009; 2011).

A. Blood sample preparation

The blood sampling protocol was approved by the Southeast London Ethics Committee (ref: 10/H0804/21) and the Cyprus National Bioethics Committee (ref: EEBK/EII/2016/18). Samples were collected from a healthy population into vacuum tubes (BD) coated with 1.8 mg/ml EDTA. The RBCs were washed twice in Phosphate Buffered Saline (PBS), centrifuged at 3000 rpm, and resuspended in PBS containing D2000 (5 g/l). The haematocrit was adjusted to 25% by volume considered physiological for the microchannel dimensions used (Lipowsky *et al.*, 1980a; 2005). For consistency, experiments were conducted with a single sample.

B. Flow configuration

The T-junction microchannel used (Epigem, Redcar, UK) had a width of $W = 100 \mu\text{m}$ and depth $D = 40 \mu\text{m}$ (Fig. 1). The pressure-driven flow was led to the open outlet reservoirs through the parent branch and the distribution of the flow between the outlet branches was controlled by adjusting the height of the outlet reservoirs using micrometer stages. RBC sedimentation in the inlet reservoir was minimised by continuously stirring the sample therein using a magnetic bar. The origin of the coordinate system is placed at the intersection of

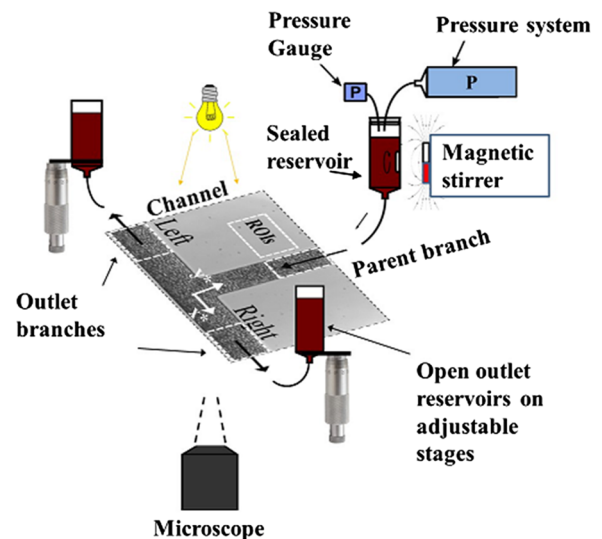


FIG. 1. The experimental apparatus used in the study, consisting of the T-type microchannel, the inlet and outlet reservoirs, and the pressure system. The components were coupled with an inverted microscope and images were acquired with a fast camera. A magnetic stirrer was used in the inlet reservoir to minimize RBC sedimentation.

the parent and daughter (outlet) branches. The coordinates are normalised with the channel width, $x^* = x/W$ and $y^* = y/W$, and thus the parent branch width spans from $x^* = -0.5$ to 0.5 and the daughter branches from $y^* = -0.5$ to 0.5 .

C. Microscopy

The microchannel was mounted on the stage of an inverted microscope (Leica DM ILM, Germany), with the focal plane set to the centre of the channel. A halogen light-source illuminated the sample and images were acquired using an IDT X3 CMOS camera (Tallahassee, USA, 125 Hz) achieving a spatial resolution of $0.65 \mu\text{m}/\text{pixel}$. Multi-pass ensemble averaged PIV processing was carried out on each of the data sets using JPIV software (www.jpiv.vennemann-online.de/) and RBCs as tracers. The flow ratio Q^* was defined as the ratio between the flow rate in the daughter and the parent branch, $Q^* = Q_D/Q_P$, and was estimated from the spatially averaged velocities (U), according to $Q^* = U_D/U_P$, for identical cross-sectional areas, with subscripts D and P indicating daughter and parent branch, respectively. The velocities U_D and U_P were calculated from the derived velocity fields.

D. Viscosity models

Generalized Newtonian, shear-dependent, blood viscosity equations are available in the literature (Yilmaz and Gundogdu, 2008). For the characterization of blood viscosity at the local scale, however, it is deemed more appropriate to adopt a constitutive model for blood that considers structural information. In general, the structural variables in such models are shear- and time-dependent functions, which provide an effective aggregate size, as the main variable of the viscosity equation. One of the candidate structure-dependent models for blood is the one developed by Quemada (1993) and its subsequent versions (Quemada, 1999 and Berli and Quemada, 2001),

$$\eta_r(t) = \eta_{r\infty} [1 - (1 - \chi)S(t, \dot{\gamma})]^{-2}, \quad (1)$$

where

$$\chi = \pm \left[\frac{\eta_{r\infty}}{\eta_{ro}} \right]^{1/2},$$

$\eta_{r\infty}$ and η_{ro} are the limiting viscosities and $S(t, \dot{\gamma})$ is the structural variable. Other models of similar nature and varying complexity exist in the literature (Owens, 2006 and Moyers-Gonzalez *et al.*, 2008). The structural variables in the aforementioned models are based on a fragmentation-coagulation equation, which assumes binary interaction and symmetry of aggregates. Another model developed by the authors (Kaliviotis and Yianneskis, 2009; 2011) is of similar nature to the aforementioned ones in that it uses the Smoluchowski fragmentation-coagulation equation for the formulation of the structural variable and the evolution of aggregates. In addition, the model incorporates the network parameter V_N , which accounts for secondary aggregation effects, such as network formation, and it does not include a zero shear limiting viscosity value. Hence, it was therefore decided to utilise this model for the estimation of the local viscosity η_e characteristics in the flow

$$\eta_e = A_i \eta_c \left(1 - e^{-\frac{1}{2\eta_c} V_N^2} \right) + \eta_d H^{Q_2} e^{-\frac{1}{2\eta_c} V_N^2} + \frac{A_i}{\dot{\gamma}} \left(\frac{H}{A^*} \right) + \eta_p. \quad (2)$$

The effective viscosity η_e is based on the energy rate model proposed by Skalak and Chien (1983) describing the external work rate done on the flowing blood, as a balance between the strain, kinetic, dissipation, and adhesion energy rates. According to the analysis in Kaliviotis and Yianneskis (2009; 2011) four terms stem out from the Skalak and Chien model describing the effective viscosity of blood. The first term accounts for viscoelastic effects attributed mainly to the secondary aggregation phenomena (aggregated network) present in physiological RBC concentrations and at low shear rates. This term depends on the aggregation intensity (A_i), the cytoplasmic viscosity of the RBC (η_c), and a network parameter V_N . The second term incorporates the viscous dissipation due to RBC membrane characteristics; this dissipation per unit volume is expected to be proportional to RBC membrane viscosity, η_d , and the number of cells in the fluid volume (and therefore proportional to the haematocrit H). The contribution of the second term is expected to decrease as the aggregate network evolves since the RBC tumbling and tank-treading motion, deformation, and cell-cell interactions are largely minimised in this condition. The third term considers the energy needed to separate RBCs in contact: the stresses required to separate such RBCs are inversely proportional to the area of contact (Chien *et al.*, 1977). Therefore, in this model, the adhesive stress is inversely proportional to the aggregate size A^* and proportional to the intensity of aggregation A_i and RBC concentration H .

The network parameter V_N has been defined as an aggregate size dependent function $V_N = \frac{B_s}{A^*}$ where $B_s = 1 + (A^* - A_{crit}^*)$ is the inter-aggregate branch size evolution and A^* is the aggregate size. Both parameters B_s and A^* are shear- and time-dependent functions that have been formulated based on the solution of the Smoluchowski coagulation-fragmentation equation (Chen and Huang, 1996 and Owens, 2006). The unity in B_s , which sets a minimum branch size of one, has been dropped in the present case, as RBC contact areas can indeed be smaller than one RBC diameter (Kaliviotis *et al.*, 2011); this results in $V_N = 1 - \frac{A_{crit}^*}{A^*}$. In the present work, the following conditions have been set in order to incorporate the experimental data:

$$V_N = 1 - \frac{A_{crit}^*}{A^*}, H \geq 0.2, A_{crit}^* \geq 5, \quad (3)$$

$$V_N = 0, H < 0.2, A_{crit}^* < 5,$$

i.e., network formation occurs above a local haematocrit of 20% and a critical aggregate size value ($A_{crit}^* = 5$).

In order to implement the viscosity model in Eq. (2), three important input parameters are required: the aggregate size A^* , haematocrit H , and shear rate $\dot{\gamma}$ (dimensionless in the model). The distributions of these parameters within the flow are determined from the experimental data in the present work, whereas the values of the remaining dimensionless constant parameters are the same as in Kaliviotis *et al.* (2011): $\eta_c = 5$ [-], $\eta_d = 10$ [-], $\eta_p = 1$ [-], experimental constant $Q_2 = 1.5$ [-], $A_i = 3$ [-].

The results produced by utilising the above-described viscosity equation were compared with those produced in a previous work (Sherwood *et al.*, 2012b), where the haematocrit-dependent viscosity model developed by Pries *et al.* (1992)

was used to calculate the viscosity profiles

$$\eta_{rel}(y^*) = 1 + 3.54[(1 - aI^*(y^*))^{-0.743} - 1]. \quad (4)$$

The constant values of 3.54 and -0.743 have been selected from the tabulated data, accompanying the Pries *et al.* viscosity model, according to the hydraulic diameter of the microchannel ($57 \mu\text{m}$). a is a calibrating factor defined as

$$a = \frac{1}{H_T} \int_{-0.5W}^{0.5W} (1 - I^*(y)) dy, \quad (5)$$

with H_T being the tube haematocrit (assumed 25%). $I^*(y)$ is the intensity profile, normalised with the maximum intensity (time-averaged) value.

The difference between the above-mentioned models lies in the distinct incorporation of aggregation effects in the Kaliviotis and Yianneskis equation (2), which include key aspects of the phenomenon such as aggregation intensity (A_i), aggregate size evolution (A^*), and network characteristics (V_N). The Pries *et al.* model has been

derived from experimental observations, including whole blood; it is thus expected that any RBC aggregation influence may be absorbed within the tabulated experimental constants.

E. Aggregate size characterisation

An edge detection algorithm was employed to determine the size of the aggregates in the flow from the acquired images (Kaliviotis *et al.*, 2016a; 2017). It consists of the following main image processing stages:

Image pre-processing to improve image quality: this involves intensity transformations and correction of uneven illumination using a Gaussian function (Sherwood *et al.*, 2014).

*Local intensity gradient (∇I_i) identification using a Prewitt-based method (Gonzales *et al.*, 2004):* the magnitude of the local intensity gradient is calculated by applying spatial convolution on a 3×3 pixel window, per unit space ΔS : $\Delta S = 1$ for the horizontal and vertical neighbouring points, and $\Delta S = \sqrt{2}$ for the diagonal neighbouring points,

$$\nabla I_i = \sqrt{\frac{\Delta I_{(i,j+1)-(i,j-1)}^2}{\Delta S^2} + \frac{\Delta I_{(i+1,j)-(i-1,j)}^2}{\Delta S^2} + \frac{\Delta I_{(i+1,j+1)-(i-1,j-1)}^2}{\Delta S^2} + \frac{\Delta I_{(i+1,j-1)-(i-1,j+1)}^2}{\Delta S^2}}. \quad (6)$$

∇I_i is normalised by the mean intensity of the convolved region (\bar{I}_{con}), $\nabla I_i^* = \frac{\nabla I_i}{\bar{I}_{con}}$, to remedy the background intensity influence on the gradients.

Blurring correction of the extreme ends of the branches; a mean contrast image ($n = 2000$) is created and the local coefficient of variation of the pixel intensity calculated ($CV_{\bar{I}_{con}} = \sigma_{\bar{I}_{con}} / \bar{I}_{con}$) using a 3×3 convolution window. $CV_{\bar{I}_{con}}$ is normalised with its maximum value in the channel ($CV_{\bar{I}_{con}}^* = \frac{CV_{\bar{I}_{con}}}{CV_{\bar{I}_{con-max}}}$) producing an image with pixel values equal to 1, for the unaffected regions, and pixel values lower than 1 for the blurred regions (~ 0.87 was the minimum value). The affected gradients in the blurred regions are corrected using the following

equation:

$$\overline{\nabla I_i^*} = \nabla I_i^* (2 - CV_{\bar{I}_{con}}^*). \quad (7)$$

Edge detection: $\overline{\nabla I_i^*}$ data above a certain threshold are defined as edge points and converted to white (assigned a value of 1). Interconnected edge pixels form the structures which count as the aggregate size A . Below the threshold value, the pixels are assigned a value of 0. The calibration of the gradient threshold value is performed in non-aggregating cases [see Figs. 2(c) and 2(d)] and used blindly in the aggregation cases [see Figs. 2(a) and 2(b)]; it involves the identification of a $\overline{\nabla I_i^*}$ value that would result in a mean edge area equal to a characteristic area of one RBC ($A_c = 15 \mu\text{m}^2$)

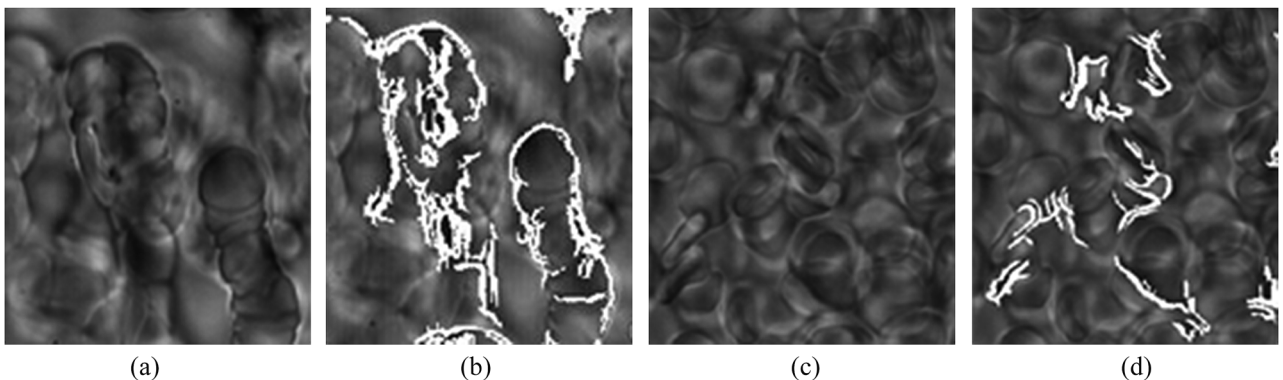


FIG. 2. [(a) and (c)] Details of the captured images for an aggregating and a non-aggregating sample. [(b) and (d)] The identified structures after image processing.

(Kaliviotis *et al.*, 2017). The identified structure sizes are normalised by A_c to provide the dimensionless aggregate size A^* in an image, with $A^* = 1$ for the characteristic edge size of one RBC. Note that the major factor influencing the effectiveness of the image processing for the calculation of the aggregate size A^* is the depth of focus, which extends in the entire depth of the channel. This results in overlapping cells and aggregates appearing in the image which is addressed by adjusting the parameters of the algorithm for conservative processing. A drawback of this approach, however, is a lower density of detected structures [apparent in Fig. 2(d)], compared to the actual number of cells in the flow.

Noise elimination: Detected edges smaller than 50% of the characteristic RBC edge area are discarded as noise.

F. Haematocrit profiles

Haematocrit profiles were calculated from the data in Sherwood *et al.* (2012b) (the same cases examined in the present study) using a non-linear intensity-dependent haematocrit function ($H_{n,l}$) developed in Sherwood *et al.* (2014)

$$H_{n,l}(I^*) = \frac{-1}{b} \ln\left(1 - \frac{I^*}{a}\right). \quad (8)$$

The values of the parameters a and b were defined in Sherwood *et al.* (2014) after calibration ($a = 0.685$, $b = 9.244$) in a $50 \times 50 \mu\text{m}$ rectangular microchannel.

G. Shear field calculations

The micro PIV technique utilised in the present study provides the velocity field calculated from the in-plane field of view. The shear rate magnitude at each location was calculated from the strain components obtained from the μPIV data by using a circulation method of differencing, as in Kaliviotis *et al.* (2011), and neglecting the out-of-plane velocity components

$$|\dot{\gamma}| = \left[2\left(\frac{\partial u}{\partial x}\right)^2 + 2\left(\frac{\partial v}{\partial y}\right)^2 + \left(\frac{\partial v}{\partial x} + \frac{\partial u}{\partial y}\right)^2 \right]^{1/2}. \quad (9)$$

Due to the lack of out-of-plane velocity information, and consequently the shear field in the depth direction, an alternative approach for the estimation of the effective shear field in the microchannel was also adopted in the present work, based on the methodology developed by Natsume and Yoshimoto (2013). In this study, the size of shear-sensitive aggregative particles was estimated as a function of shear rate in simple shear flows, allowing the aggregates to be used as shear probes. The dependency of the RBC aggregation phenomenon on the shear rate is very well established in the literature [see, for example, the studies of Snabre and Mills (1996)]. Therefore in the present study, the size of RBC aggregates was estimated in simple Couette flows using a plate-plate shearing system (LINKAM CSS450) for a range of shear rates [a schematic of the geometry is provided in Fig. 3(a)]. The shear rate was calculated at the radius of observation, $R = 7.5 \text{ mm}$, according to the angular velocity of the bottom plate ω and the gap ($h = 40 \mu\text{m}$) between the plates, $\dot{\gamma} = \frac{R\omega}{h}$. The following sigmoidal function was used to fit the data in

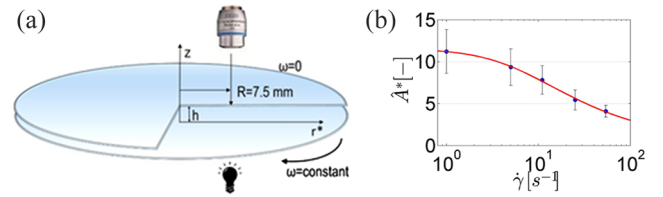


FIG. 3. (a) A schematic of the plate-plate geometry. (b) The mean aggregate size \hat{A}^* calculated at different shear rates in the plate-plate system from 250 images. The error bars indicate the standard deviation of the mean. The aggregate size \hat{A}^* is normalised by the characteristic size of one RBC.

Matlab [Fig. 3(b)]

$$\frac{\hat{A}^*(\dot{\gamma}) - \hat{A}_\infty^*}{\hat{A}_0^* - \hat{A}_\infty^*} = \left[1 + (\dot{\gamma}\lambda)^a \right]^{\frac{n-1}{\alpha}}, \quad (10)$$

with $\hat{A}_0^* = 12$ (the zero-shear size), $\hat{A}_\infty^* = 1$ (the high-shear size), and $\lambda = 0.16$, $\alpha = 1.23$, and $n = 0.5$ (the parameters of the function). \hat{A}^* is the ensemble average (in time and space) of the aggregate size calculated from 250 images and normalised by the characteristic size of one RBC. Details of the processed images are shown in Fig. 2. The shear field for the microchannel flows was extracted using Eq. (10), when $\dot{\gamma}$ was made the subject of the equation [i.e., $\dot{\gamma} = \dot{\gamma}(\hat{A}^*)$], utilising the \hat{A}^* values determined from the processed images.

H. Statistical analysis

The aggregate size and mean image intensity are typically expressed in terms of spatially and/or temporally averaged values. For the exponentially distributed data of aggregate size, the mean values were obtained using a least squares fitting function implemented in Matlab (Demirkaya *et al.*, 2005).

III. RESULTS

Figures 4(a) and 4(b) illustrate the velocity field $V(x^*, y^*)$ for two extreme flow ratio cases: $Q^* = 0.6/0.4$ and $Q^* = 0.972/0.028$. The vector size and density in the velocity field plots are altered for visualisation purposes. The magnitude of the local shear rate, calculated using Eq. (9), is shown in panels (c) and (d) and the distribution of the aggregate size \bar{A}^* for the same cases is shown in panels (e) and (f). Note that \bar{A}^* sizes below 3 have been omitted in the contour plot, in order to focus on the behaviour of larger aggregates in the flow.

The velocity and corresponding shear rate fields are dependent on the flow partitioning and are characterised by small near-wall velocities (and hence high shear), stagnation sites at the wall opposite the parent branch, and regions of higher shear rate in the vicinity of the T-junction as expected. The aggregate size \bar{A}^* plots in panels (e) and (f) show that, in general, larger aggregates tend to appear in regions of low in-plane shear [panels (c) and (d)]; they are located along the centreline in the parent branch and towards the wall (opposite the parent) in the daughter branches. It is, however, apparent that the aggregate size slightly increases in the vicinity of the T-junction, although the strain rate in this region increases to about 20 s^{-1} from near zero in the parent branch centreline.

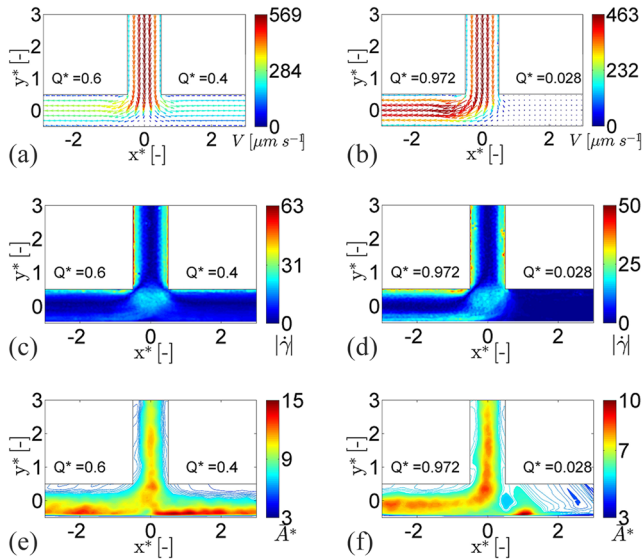


FIG. 4. Panels (a), (c), and (e) show velocity, strain rate, and aggregate size distribution, respectively, for a flow ratio of $\sim 0.6/0.4$. Panels (b), (d), and (f) show velocity, strain rate, and aggregate size distribution, respectively, for a flow ratio of $\sim 0.972/0.028$.

The fact that aggregates appear to retain their size as they encounter the T-junction despite a change in the shear of the order of ~ 20 to 25 s^{-1} is surprising and counterintuitive; in accordance with the current understanding of the RBC aggregation phenomenon, the aggregate size scales inversely with the shear rate (Baskurt and Meiselman, 2003).

The aforementioned behaviour can be explained by first considering the time-dependency of the aggregation phenomenon and, more specifically, the time-response of aggregation (or disaggregation) to changes in the flow conditions. Aggregation is a time-dependent phenomenon, with characteristic times in the order of 5–7 s (Cokelet, 1980 and Kaliviotis and Yiannakis, 2008). The maximum velocity in the parent branch is observed to be above $400 \mu\text{m s}^{-1}$ in both cases examined in Fig. 4, and the distance from the end of the parent branch to the region of high shear is approximately $50 \mu\text{m}$; this results in a transit time of less than a second, not sufficient time for disaggregation of the ensuing aggregates. Therefore, the latter retain their size as they transit through the increased shear, flow partitioning region.

Second, aggregates exhibit elastic/viscoelastic behaviour due to the RBC membrane properties, and therefore alterations in their shape characteristics without dispersion should be expected when subjected to shearing forces. Indeed, in the vicinity of the T-junction, aggregates are subjected not

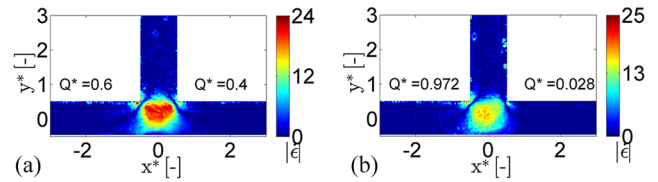


FIG. 5. Extensional strain rate for the two cases shown in Fig. 4.

only to shearing stresses but also to substantial stretching. Figure 5 illustrates the magnitude of the extensional strain rate in the region near the T-junction. Extensional strain rates vary between 15 and 25 s^{-1} in the junction, i.e., levels similar to those seen in Figs. 4(c) and 4(d), confirming that linear deformation dominates in this region. The slight increase in the size of aggregate structures observed in this region may be due to the stretching they experience as they travel through the extensional flow field therein.

Evidence of such stretching of aggregates in the vicinity of the bifurcation is provided in Fig. 6 below, showing a sequence of images of aggregating RBCs in a low concentration suspension entering the bifurcation at a flow ratio of approximately 0.5.

Selected distributions of aggregate size, haematocrit, and viscosity, estimated for a flow ratio of 0.52 and 0.48 in the left and right daughter branches, respectively, are presented in contour form in Fig. 7. The aggregate size \bar{A}^* shown in panel (a) is the local mean value of A^* averaged in time (250 images). A maximum aggregate size of around 10 (i.e., the edge area of 10 RBCs) can be observed in this case located in the lower Q^* branch. Note that the colourless region in the plot indicates \bar{A}^* values close to one RBC (i.e., dispersed aggregates), not shown in the color bar. In Fig. 7(b), the distribution of the local haematocrit appears symmetric in the parent branch. However, this not the case for the distribution in daughter branches; an asymmetry (skewness towards the walls) and a slight increase of the haematocrit towards the branch of the high flow rate branch can be observed—characteristics that have been examined in detail in previous studies (Pries *et al.*, 1989; Sherwood *et al.*, 2012b; and 2014). The shear distribution for this particular case, calculated from Eq. (10), is shown in Fig. 7(c) and the calculated viscosity field in Fig. 7(d). The shear distribution is qualitatively similar to the aggregate size distribution as expected since the aggregate size is used as a shear probe in this study; a local shear minimum is observed at the point that the flow enters the low flow branch due to the larger aggregates observed therein. Qualitative differences when comparing the shear field with those of

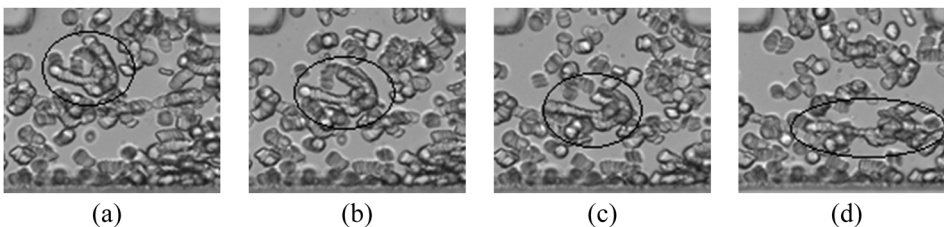


FIG. 6. Aggregate stretching in the vicinity of the bifurcation for a dilute concentration of RBCs suspended in Dextran 2000 (5 g/l).

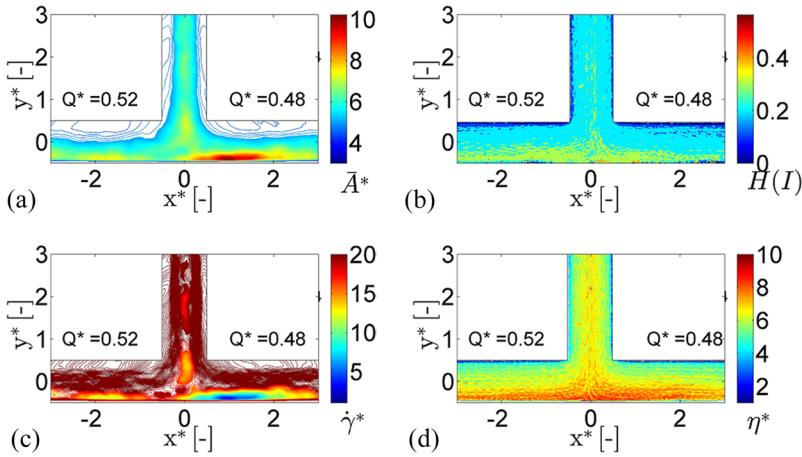


FIG. 7. Representative results for the case $Q^* = 0.52$ and 0.48 in the left and right branches, respectively. Averaging has been made for 250 images. (a) The aggregate size distribution. (b) The haematocrit field. (c) The shear rate distribution [Eq. (10)]. (d) The calculated viscosity.

Fig. 4 include the fact that the minimum shear does not appear in the centre of the flow in the parent branch, and that there is a slight decrease in the shear magnitude in the bifurcation region relative to that upstream in the parent branch.

The viscosity distribution follows the haematocrit trends, with higher viscosities present near the bottom wall of the outlet channels. A slightly wider region of high viscosity can be detected in the location of the maximum aggregate.

In order to examine the sensitivity of the aforementioned approach to capture the variation in viscosity with flow conditions, local viscosity distributions are plotted for various flow ratios in Fig. 8. The general dependency of the viscosity on the flow ratio in the daughter branches is better illustrated when considering two extreme cases [Figs. 8(a) and 8(f)]; the viscosity in the branch of the highest flow ratio appears elevated compared to that of the low flow ratio branch. In the parent branch, the viscosity distribution appears to be symmetric with higher values present in the central parts of the flow, in all cases, as expected. The flow rate in this branch is almost constant, and the downstream flow conditions do not seem to influence the viscosity characteristics in the parent branch.

At the outlets of the daughter branches (i.e., within the ROIs—please see Fig. 1), the viscosity characteristics appear fully developed in the flow direction. A strong asymmetry in the viscosity profiles is observed therein, for low flow ratios, with the maximum magnitude appearing close to the

walls of the channel. It can also be observed that in closer proximity to the walls within these regions, the viscosity is lower than the maximum observed in the channel in each particular case.

To examine the observations made above in more detail, the viscosity profile across the flow was calculated within the ROIs shown in Fig. 1 for all flow ratios tested in this work and presented in Fig. 9. The minimum viscosity magnitude is located on the walls of the outlet branches adjacent to the parent branch (at $y^* = 0.5$) for all flow ratios, and increased viscosity appears close to the walls opposite the parent branch for the intermediate Q^* cases (0.25–0.75). Viscosity profiles become symmetric as the flow ratio approaches 1.

Qualitatively the results agree with those presented in our previous work (Sherwood *et al.*, 2012b), where the haematocrit-dependent viscosity model developed by Pries *et al.* (1992) [Eq. (3)] was used to calculate the viscosity profiles of the same data analysed in the present work. However, the results from the two approaches differ in (a) the maximum viscosity magnitude which is higher by approximately a factor of 4 in the present work compared to that in (Sherwood *et al.*, 2012b) and (b) the distribution of viscosity in the cross flow direction (y^*) which appears to be sharper close to the channel wall in the present study. These differences are better illustrated in Fig. 10 comparing the viscosity profiles averaged for Q^* in the range 0.45–0.55 obtained in the present work with those in Sherwood *et al.* (2012b) for both aggregating and non-aggregating samples.

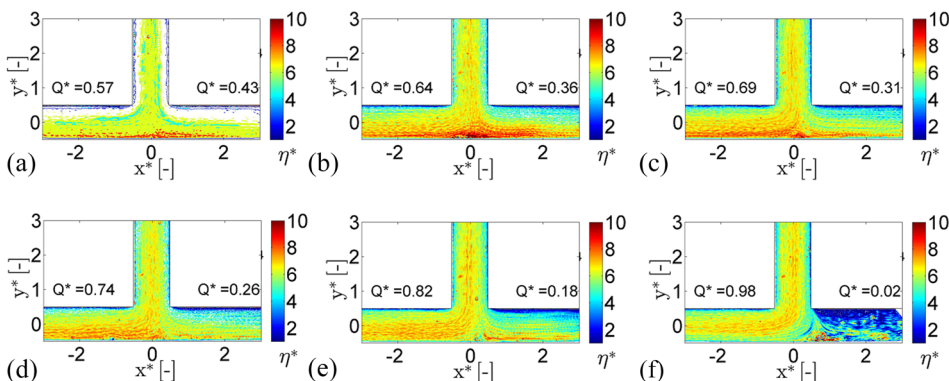


FIG. 8. Local viscosity distributions for various flow ratio cases.

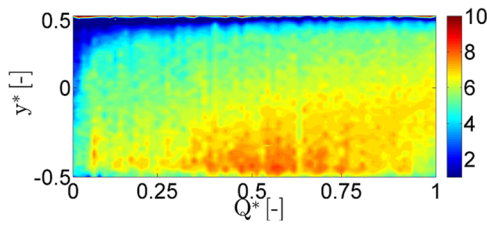


FIG. 9. Viscosity distribution in the cross-flow (y^*) direction, spatially averaged in the direction of the flow (x^*) within the ROIs, for all the flow ratios tested.

The viscosity data have been normalised with their maximum values for direct comparison.

The differences between the two viscosity estimation approaches can be attributed to RBC aggregation and resulting microstructure, and its implication on haematocrit and viscosity. In particular, Fig. 10 highlights two key aspects of RBC aggregation: first, the influence of RBC aggregation on the haematocrit distribution and second the direct contribution of aggregation to viscosity. The viscosity data in Sherwood *et al.* (2012b) are based on the Pries viscosity model which does not account explicitly for RBC aggregation. Thus, the maximum magnitude of viscosity for the non-aggregating case in Fig. 10 appears on the wall of the channel (at $y^* = -0.5$), whereas for the aggregating case, at a considerable distance away from the wall. At both channel walls, the relative viscosity is lower for the aggregating case. The comparison between the viscosity profiles in the present study and that in Sherwood *et al.* (2012b) also shows that the slope of the viscosity gradient in the y^* direction near the wall differs and is found lower in the aggregating data of Sherwood *et al.*

The second aspect concerning the influence of RBC aggregation on the local viscosity characteristics regards the direct contribution of aggregation in addition to the haematocrit effects. This effect is captured in the viscosity curve produced in the present work (black circles in Fig. 10), as the viscosity equation (2) is both haematocrit- and RBC aggregation-dependent. The main qualitative differences when comparing to the curve of the aggregating sample produced in Sherwood *et al.* (2012b) include a sharper profile close to the channel wall (at $y^* = -0.5$), a smaller distance of the maximum magnitude from the wall, and the variation of the viscosity within the core of the flow. The maximum relative viscosity

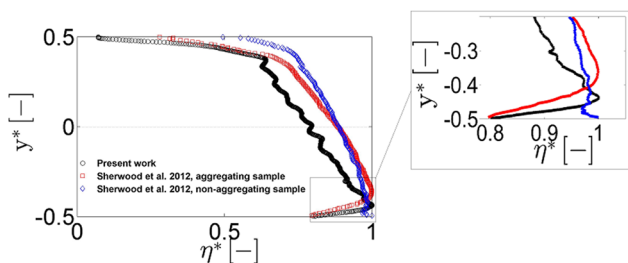


FIG. 10. Comparison of viscosity profiles averaged for Q^* in the range 0.45–0.55. The red (square) and blue (diamond) data are the results showed in the work of Sherwood *et al.* (2012b), where the Pries viscosity model was used. The black (circles) data are the viscosity profile calculated in the present work. The companion figure illustrates the details of the curves near the maximum values.

values in the wall at $y^* = -0.5$ appear the same, whereas a difference is observed at walls adjacent to the parent branch ($y^* = 0.5$).

The area near the T-junction of the bifurcating channel is of particular interest. The distribution of viscosity in Fig. 8 showed that the maximum viscosity magnitude appears concentrated in this region, and in particular on the walls of the channel opposite the parent branch. This is expected, as the stagnation regions develop near these locations, depending on the flow ratio in the daughter branches. In order to identify the exact location of the maximum viscosity magnitude in the x^* direction, the viscosity values were averaged in the y^* direction for all x^* for each flow ratio, and the x^* location of the maximum viscosity value was identified and plotted in Fig. 11 as a function of flow ratio. As the figure illustrates, for the cases of equal flow split (Q^* near 0.5), the location of maximum viscosity is opposite the parent branch central axis ($x^* = 0$). However, when the flow is unevenly distributed in the daughter branches, the maximum viscosity is observed biased towards the side of the higher flow rate branch ($-1 < x^* < 0$). This tendency is more clear for the lower flow ratios ($Q^* < \sim 0.2$).

The local viscosity behaviour, as influenced by the RBC aggregation phenomenon and described herein, has important implications in both physiology and pathology. The maximum increase in the viscosity magnitude by a 4-fold found in this study compared to our previous results depends not only on the detected aggregate sizes in the channel but also on the parameters used in the viscosity equation (2). This increase should be expected according to our current understanding of the RBC aggregation/blood viscosity relationship (Baskurt and Meiselman, 2003). Indeed, when RBC aggregation is increased in the *in vivo* examination of vascular resistance, an increase in the later is initially observed (Baskurt, 2008). Hemorheological alterations have considerable impact on various pathologies, such as atherosclerosis, ischemia states, hypertension, and cerebrovascular implications. (Toth *et al.*, 2007); this impact is typically manifested at a local level; for example, a negative correlation has been established between RBC aggregation and cerebral blood flow (Ajmani *et al.*, 2000 and Toth *et al.*, 2007). However, in the present work, physiological levels of RBC aggregation are considered and as a result, no adverse impact on the flow of blood is expected. The maximum viscosity magnitude observed in all cases ($\eta^* \sim 8$) is well below the yield stress levels (typically $\eta^* \gg 100$ at low shear rates) despite the fact that stagnation regions exist in the vicinity of the T-junction (Lee *et al.*, 2011). Also the minimum viscosity found in the very low flow ratio branches

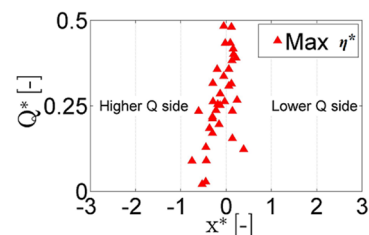


FIG. 11. The location of maximum viscosity magnitude in the outlet branches (x^* direction) for all Q^* cases.

approaches the order of magnitude of the plasma viscosity ($\eta^* \sim 1$).

The present findings have implications for modeling of microscale blood flows and might be useful in the design of both diagnostic applications and targeted drug delivery systems. Continuum modeling approaches make use of either a constant haematocrit or non-Newtonian models which might underestimate the effect of aggregation on viscosity highlighted here. Many point-of-care diagnostics take advantage of the plasma skimming phenomena, for example, for cell separation and the latter would depend on the viscosity distribution in the presence of aggregation reported herein. Similarly, in drug delivery systems, significant interaction of drug carriers with red blood cells takes place from the point of injection until the drug reaches the target site. This transport involves various scales of the circulation (Lee *et al.*, 2013) and is a major design consideration. The objective for an effective drug delivery is to achieve sufficient margination of the drug particles from the core of the flow to the diseased site. However, the influence of RBC aggregation on particle margination has not been examined in depth in the literature. The present study can aid understanding of the relevant processes in drug delivery; in conditions where RBC aggregation is present, the viscosity will be elevated; hence, the migration of the particles toward the walls would be negatively influenced. Finally, although the emphasis in this paper is on microhaemodynamics, the local variation of viscosity demonstrated here is important in other microsystems involving soft particle suspensions, for example, 3D printing applications.

IV. CONCLUSIONS

In the present work, the local viscosity distribution for aggregating blood samples flowing in a rectangular T-junction microchannel was examined. The viscosity model used in this work required information on the local haematocrit, aggregate size, and shear rate, which was obtained from the experimental data. Information on aggregation intensity, cytoplasmic, membrane, and plasma viscosities, was obtained from the literature. The shear field was estimated based on the relationship between aggregate size and shear rate established from additional shearing experiments in a constant shear device due to the lack of out-of-plane shear information in the velocity measurements.

The results confirmed earlier observations and claims on the apparent viscosity behaviour of the blood flowing in the microscale and revealed new information regarding the spatial characteristics of viscosity in the bifurcating microchannel geometry. Two main observations arise from this study; the viscosity in the branch of the lower flow rate is not significantly elevated, and the maximum viscosity magnitude appears towards the side of the higher flow rate branch. These observations may help us to understand why the effects of physiological aggregation intensity do not negatively impact microcirculatory flows. Indeed, the general understanding regarding the relationship between RBC aggregation and blood flow is that it increases the viscosity in low shear rates which is in contrast to what the study demonstrates. Further work is required to clarify this behaviour by perhaps examining the

viscosity distribution in more complex networks of channels and in more intense aggregation states.

ACKNOWLEDGMENTS

The authors would like to thank Dr. Peter Vennemann for providing the free PIV analysis software JPIV (www.jpiv.vennemann-online.de). The study has been partly supported with funding from the internal Start-Up Grants of the Cyprus University of Technology.

- Ajmani, R. S., Metter, E. J., Jaykumar, R., Ingram, D. K., Spangler, E. L., Abugo, O. O., and Rifkind, J. M., "Hemodynamic changes during aging associated with cerebral blood flow and impaired cognitive function," *Neurobiol. Aging* **21**(2), 257–269 (2000).
- Baskurt, O. K., "In vivo correlates of altered blood rheology," *Biorheology* **45**(6), 629–638 (2008).
- Baskurt, O. K. and Meiselman, H. J., "Blood rheology and hemodynamics," *Semin. Thromb. Hemostasis* **29**(5), 435–450 (2003).
- Berli, C. L. A. and Quemada, D., "Aggregation behavior of red blood cells in shear flow. A theoretical interpretation of simultaneous rheo-optical and viscometric measurements," *Biorheology* **38**(1), 27–38 (2001).
- Brands, J., Kliner, D., Lipowsky, H. H., Kameneva, M. V., Villanueva, F. S., and Pacella, J. J., "New insights into the microvascular mechanisms of drag reducing polymers: Effect on the cell-free layer," *PLoS ONE* **8**(10), e77252 (2013).
- Chen, J. and Huang, Z., "Analytical model for effects of shear rate on rouleau size and blood viscosity," *Biophys. Chem.* **58**(3), 273–279 (1996).
- Chien, S., Sung, L. A., Kim, S., Burke, A. M., and Usami, S., "Determination of aggregation force in rouleaux by fluid mechanical technique," *Microvasc. Res.* **13**(3), 327–333 (1977).
- Cokelet, G. R., "Rheology and hemodynamics," *Annu. Rev. Physiol.* **42**, 311–324 (1980).
- Damiano, E. R., Long, D. S., and Smith, M. L., "Estimation of viscosity profiles using velocimetry data from parallel flows of linearly viscous fluids: Application to microvascular haemodynamics," *J. Fluid Mech.* **512**, 1–19 (2004).
- Demirkaya, O., Asyali, M. H., and Shoukri, M. M., "Segmentation of cDNA microarray spots using Markov random field modeling," *Bioinformatics* **21**(13), 2994–3000 (2005).
- Gonzales, R., Woods, R., and Eddins, S., *Digital Image Processing Using Matlab* (Prentice Hall, Upper Saddle River, New Jersey, 2004).
- Kaliviotis, E. and Yianneskis, M., "Fast response characteristics of red blood cell aggregation," *Biorheology* **45**(6), 639–649 (2008).
- Kaliviotis, E. and Yianneskis, M., "An energy-rate based blood viscosity model incorporating aggregate network dynamics," *Biorheology* **46**(6), 487–508 (2009).
- Kaliviotis, E. and Yianneskis, M., "Blood viscosity modelling: Influence of aggregate network dynamics under transient conditions," *Biorheology* **48**(2), 127–147 (2011).
- Kaliviotis, E., Dusting, J., and Balabani, S., "Spatial variation of blood viscosity: Modelling using shear fields measured by a μ PIV based technique," *Med. Eng. Phys.* **33**(7), 824–831 (2011).
- Kaliviotis, E., Dusting, J., Sherwood, J. M., and Balabani, S., "Quantifying local characteristics of velocity, aggregation and hematocrit of human erythrocytes in a microchannel flow," *Clin. Hemorheol. Microcirc.* **63**(2), 123–148 (2016a).
- Kaliviotis, E., Pasiyas, D., Sherwood, J. M., and Balabani, S., "Red blood cell aggregate flux in a bifurcating microchannel," *Med. Eng. Phys.* **48**, 23 (2016b).
- Kaliviotis, E., Sherwood, J. M., and Balabani, S., "Partitioning of red blood cell aggregates in bifurcating microscale flows," *Sci. Rep.* **7**, 44563 (2017).
- Koutsiaris, A. G., "Correlation of axial blood velocity to venular and arteriolar diameter in the human eye in vivo," *Clin. Hemorheol. Microcirc.* **61**(3), 429–438 (2016a).
- Koutsiaris, A. G., "Wall shear stress in the human eye microcirculation in vivo, segmental heterogeneity and performance of in vitro cerebrovascular models," *Clin. Hemorheol. Microcirc.* **63**(1), 15–33 (2016b).
- Leble, V., Lima, R., Dias, R., Fernandes, C., Ishikawa, T., Imai, Y., and Yamaguchi, T., "Asymmetry of red blood cell motions in a microchannel with a diverging and converging bifurcation," *Biomicrofluidics* **5**(4), 044120 (2011).

- Lee, B., Xue, S., Nam, J., Lim, H., and Shin, S., "Determination of the blood viscosity and yield stress with a pressure-scanning capillary hemorheometer using constitutive models," *Korea Aust. Rheol. J.* **23**(1), 1–6 (2011).
- Lee, T., Choi, M., Kopacz, A. M., Yun, S., Liu, W. K., and Decuzzi, P., "On the near-wall accumulation of injectable particles in the microcirculation: Smaller is not better," *Sci. Rep.* **3**, 2079 (2013).
- Lima, R., Wada, S., Tsubota, K. I., and Yamaguchi, T., "Confocal micro-PIV measurements of three-dimensional profiles of cell suspension flow in a square microchannel," *Meas. Sci. Technol.* **17**(4), 797–808 (2006).
- Lima, R., Ishikawa, T., Imai, Y., Takeda, M., Wada, S., and Yamaguchi, T., "Radial dispersion of red blood cells in blood flowing through glass capillaries: The role of hematocrit and geometry," *J. Biomech.* **41**(10), 2188–2196 (2008a).
- Lima, R., Wada, S., Tanaka, S., Takeda, M., Ishikawa, T., Tsubota, K. I., Imai, Y., and Yamaguchi, T., "In vitro blood flow in a rectangular PDMS microchannel: Experimental observations using a confocal micro-PIV system," *Biomed. Microdevices* **10**(2), 153–167 (2008b).
- Lipowsky, H. H., "Microvascular rheology and hemodynamics," *Microcirculation* **12**(1), 5–15 (2005).
- Lipowsky, H. H., Usami, S., and Chien, S., "In vivo measurements of 'apparent viscosity' and microvessel hematocrit in the mesentery of the cat," *Microvasc. Res.* **19**(3), 297–319 (1980a).
- Lipowsky, H. H., Usami, S., Chien, S., and Pittman, R. N., "Hematocrit determination in small bore tubes from optical density measurements under white light illumination," *Microvasc. Res.* **20**(1), 51–70 (1980b).
- Long, D. S., Smith, M. L., Pries, A. R., Ley, K., and Damiano, E. R., "Microviscosimetry reveals reduced blood viscosity and altered shear rate and shear stress profiles in microvessels after hemodilution," *Proc. Natl. Acad. Sci. U. S. A.* **101**(27), 10060 (2004).
- Mehri, R., Laplante, J., Mavriplis, C., and Fenech, M., "Investigation of blood flow analysis and red blood cell aggregation," *J. Med. Biol.* **34**(5), 469–474 (2014).
- Moyers-Gonzalez, M., Owens, R. G., and Fang, J., "A non-homogeneous constitutive model for human blood. Part I. Model derivation and steady flow," *J. Fluid Mech.* **617**, 327–354 (2008).
- Natsume, T. and Yoshimoto, M., "A method to estimate the average shear rate in a bubble column using liposomes," *Ind. Eng. Chem. Res.* **52**(51), 18498–18502 (2013).
- Owens, R. G., "A new microstructure-based constitutive model for human blood," *J. Non-Newtonian Fluid Mech.* **140**(1–3), 57–70 (2006).
- Pries, A. R., Ley, K., Claassen, M., and Gaetgens, P., "Red cell distribution at microvascular bifurcations," *Microvasc. Res.* **38**(1), 81–101 (1989).
- Pries, A. R., Neuhaus, D., and Gaetgens, P., "Blood viscosity in tube flow: Dependence on diameter and hematocrit," *Am. J. Physiol.–Heart Circ. Physiol.* **263**(6), H1770–H1778 (1992).
- Pries, A. R. and Secomb, T. W., "Rheology of the microcirculation," *Clin. Hemorheol. Microcirc.* **29**(3–4), 143–148 (2003).
- Pries, A. R. and Secomb, T. W., "Microvascular blood viscosity in vivo and the endothelial surface layer," *Am. J. Physiol.–Heart Circ. Physiol.* **289**(6), H2657–H2664 (2005).
- Quemada, D., "A non-linear Maxwell model of biofluids: Application to normal blood," *Biorheology* **30**(3–4), 253–265 (1993).
- Quemada, D., "Rheological modelling of complex fluids: IV: Thixotropic and 'thixoelastic' behaviour. Start-up and stress relaxation, creep tests and hysteresis cycles," *Eur. Phys. J.: Appl. Phys.* **5**(2), 191–207 (1999).
- Sampaio, D., Lopes, D., and Semiao, V., "Horse and dog blood flows in PDMS rectangular microchannels: Experimental characterization of the plasma layer under different flow conditions," *Exp. Therm. Fluid Sci.* **68**, 205–215 (2015).
- Secomb, T. W., "Blood flow in the microcirculation," *Annu. Rev. Fluid Mech.* **49**, 443 (2017).
- Sherwood, J. M., Dusting, J., Kaliviotis, E., and Balabani, S., "The effect of red blood cell aggregation on velocity and cell-depleted layer characteristics of blood in a bifurcating microchannel," *Biomicrofluidics* **6**(2), 024119 (2012a).
- Sherwood, J. M., Kaliviotis, E., Dusting, J., and Balabani, S., "Hematocrit, viscosity and velocity distributions of aggregating and non-aggregating blood in a bifurcating microchannel," *Biomech. Model. Mechanobiol.* **13**(2), 259–273 (2012b).
- Sherwood, J. M., Holmes, D., Kaliviotis, E., and Balabani, S., "Spatial distributions of red blood cells significantly alter local haemodynamics," *PLoS ONE* **9**(6), e100473 (2014).
- Skalak, R. and Chien, S., "Theoretical models of rouleau formation and disaggregation," *Ann. N. Y. Acad. Sci.* **416**, 138 (1983).
- Snabre, P. and Mills, P., "II. Rheology of weakly flocculated suspensions of viscoelastic particles," *J. Phys. III* **6**(12), 1835–1855 (1996).
- Toth, K., Kesmarky, G., and Alexy, T., in *Handbook of Hemorheology and Hemodynamics*, Clinical Significance of Hemorheological Alterations, edited by O. K. Baskurt, M. R. Hardeman, M. W. Rampling, and H. J. Meiselman (IOS Press, 2007), pp. 392–432.
- Yilmaz, F. and Gundogdu, M. Y., "A critical review on blood flow in large arteries; relevance to blood rheology, viscosity models, and physiologic conditions," *Korea Aust. Rheol. J.* **20**(4), 197–211 (2008).